NUMERICAL ANALYSYS OF MINOR HEAD LOSSES IN 3D FLOW GEOMETRIES USING FINITE ELEMENT MODELING

Nguyen Manh Hung[1], Vu Manh Hieu[1], Ha Truong Sang[1,*]

DOI: http://doi.org/ 10.57001/huih5804.2025.244

ABSTRACT

This study presents a numerical investigation of minor head losses in three-dimensional (3D) complex geometries using the finite element method (FEM). Minor losses commonly occur due to abrupt geometric variations in hydraulic systems, leading to significant energy dissipation. Although experimental techniques have traditionally been employed to quantify such losses, they often encounter limitations in capturing intricate flow structures. With the advancements in computational power, numerical simulations have emerged as a robust alternative. In this work, FEM is applied to simulate incompressible, laminar flow of Newtonian fluids through various 3D configurations, including flow past a sphere, sudden expansions, and curved bends. The computational domain is discretized using unstructured tetrahedral and hexahedral meshes, and a semi-implicit time integration scheme is adopted. The numerical model is validated against benchmark solutions, and the minor loss coefficient is evaluated for a range of Reynolds numbers. The results demonstrate the effectiveness of FEM in accurately capturing flow separation and pressure drop in complex 3D geometries.

Keywords: *Minor head loss, laminar flow, complex geometries, FEM, CFD.*

[1]Faculty of Mechanical Engineering, Le Quy Don Technical University
[*]Email: sanght.st@lqdtu.edu.vn

Received: 04/6/2025
Revised: 22/7/2025
Accepted: 25/7/2025

1. INTRODUCTION

In hydraulic systems, minor head losses primarily occur due to geometric irregularities such as abrupt expansions, contractions, and bends, which lead to flow separation and energy dissipation. Although these losses are often neglected in simplified analytical models, these local losses can have a significant impact on the overall performance and efficiency of hydraulic machinery and components [1, 2]. Therefore, accurate estimation of minor losses is crucial for the effective design and optimization of pipelines, valves, and other hydraulic devices.

Traditionally, empirical and experimental methods have been utilized to determine minor loss coefficients [5, 6]. While experimental studies offer valuable insights into fluid behavior, they are often constrained by high costs, experimental complexity, and difficulties in reproducing arbitrary or highly intricate geometries. Consequently, computational methods have gained increasing attention in recent decades as a more flexible and cost-effective alternative for evaluating hydraulic losses.

With the advancement of computer hardware and numerical techniques, computational fluid dynamics (CFD) has emerged as an effective tool for analyzing flow behavior and quantifying head losses in complex domains [7]. For instance, Chemezov [6] applied finite volume methods to model fluid resistance in pipeline transitions, while Weber et al. [7] utilized commercial CFD software to compute pressure losses across a variety of geometric configurations.

Among numerical approaches, the finite element method (FEM) offers several advantages: it accommodates unstructured meshes, supports complex boundary conditions, and is well-suited for solving the incompressible laminar Navier-Stokes equations. Several previous studies have demonstrated the applicability of FEM for simulating two-dimensional fluid flow and calculating local loss coefficients in relatively simple geometries [8].

This study extends the FEM-based modeling framework to three-dimensional (3D) flow problems involving complex geometries, such as spheres, sudden expansions, and curved pipes. The primary objectives are to evaluate the minor loss coefficient across a range of

Reynolds numbers and to assess the accuracy and robustness of FEM in capturing key 3D flow features that influence hydraulic losses.

The remainder of this paper is structured as follows: Section 2 outlines the governing equations and numerical methodology. Section 3 presents the benchmark test cases and corresponding simulation results. Section 4 concludes the study and provides suggestions for future research.

2. METHODOLOGY

2.1. Governing equations

Assuming an incompressible flow of a Newtonian fluid, the governing equations are the incompressible Navier-Stokes equations, which can be expressed in the Eulerian framework as follows [8, 9]:

$$\begin{aligned} &\nabla\cdot\mathbf{u}=0 \quad \text{in } \Omega && \text{(a)}\\ &\rho\left[\frac{\partial\mathbf{u}}{\partial t}+\mathbf{u}\cdot\nabla\mathbf{u}\right]=\nabla\cdot\sigma \quad \text{in } \Omega && \text{(b)} \end{aligned} \tag{1}$$

where ρ, **u**, **σ** and Ω are the fluid density, the fluid velocity, the fluid stress tensor, and the fluid domain, respectively.

The fluid domain's boundary is denoted by Γ. The corresponding constitutive equations for fluid flow in Eq. (1) can be expressed as follows [10]:

$$\begin{aligned} &\sigma=-p\mathbf{I}+\tau, && \text{(a)}\\ &\tau=\mu[\nabla\mathbf{u}+(\nabla\mathbf{u})^{T}] && \text{(b)} \end{aligned} \tag{2}$$

where p, μ, **τ**, and **I** indicate the pressure, the fluid dynamic viscosity, the shear stress tensor, and the second-order identity tensor, respectively.

The description of boundary conditions is as follows:

$$\begin{aligned} &\mathbf{u}=\bar{\mathbf{u}} \quad \text{on } \Gamma_{\mathbf{u}}, && \text{(a)}\\ &\sigma\cdot\mathbf{n}=\bar{\mathbf{t}} \quad \text{on } \Gamma_{\mathbf{t}} && \text{(b)} \end{aligned} \tag{3}$$

where **n** denotes the outward unit normal vector of the fluid boundary. $\Gamma_{\mathbf{u}}$ and $\Gamma_{\mathbf{t}}$ are the boundaries where the velocity $\bar{\mathbf{u}}$ and traction $\bar{\mathbf{t}}$ are imposed on the Dirichlet and Neumann boundary conditions, respectively.

2.2. Finite element method for incompressible fluid flow

The finite element method (FEM) is a widely used technique in computational mechanics, particularly for solving problems related to thermal conduction, the Poisson equation, and the Navier-Stokes equations. FEM is especially effective in handling unstructured meshes that result from complex geometries. In this study, we employ the fractional step method [11] to solve the incompressible Navier-Stokes equations. The diffusion terms are discretized in time using the second-order implicit Crank-Nicolson scheme, while the convective terms are treated with the second-order explicit Adams-Bashforth scheme. The numerical scheme proceeds through three main steps: first, the momentum equation is solved to obtain the intermediate velocity field $\hat{u}$; next, the pressure is computed by solving the Poisson equation; and finally, the velocity is corrected using the computed pressure field.

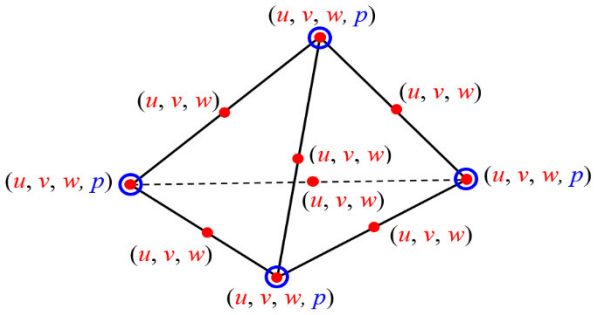

Fig. 1. Degrees of freedom assigned for the P2P1 on the tetrahedral finite element

The P2P1 finite element pair, as illustrated in Fig. 1, is employed in this study. In this element, pressure is defined at the vertices, while velocity is defined at both the vertices and the midpoints of the edges. The momentum equations are discretized using the consistent streamline upwind Petrov-Galerkin method, whereas the pressure equation is discretized using the standard Galerkin method. The weak formulations of these equations are expressed as follows [8, 11]:

Find $u\in H^1(\Omega)$, $\hat{u}\in H^1(\Omega)$ and $p\in H^1(\Omega)$ such that:

$$\begin{aligned} &\int_{\Omega} w_i\frac{\hat{u}_i-u_i^n}{\Delta t}d\Omega+\frac{\mu}{2\rho}\int_{\Omega} w_{i,j}\hat{u}_{i,j}\,d\Omega\\ &=\frac{\mu}{\rho}\int_{\Gamma_p} w_i\bar{t}_i^{u}\,d\Gamma-\frac{\mu}{2\rho}\int_{\Omega} w_{i,j}u_{i,j}^n\,d\Omega\\ &-\frac{1}{2}\int_{\Omega} w_i\left(3u_j^n u_{i,j}^n-u_j^{n-1}u_{i,j}^{n-1}\right)d\Omega \end{aligned} \tag{4}$$

$$\int_{\Omega} q_{,i}p_{,i}^{n+1}d\Omega=\int_{\Gamma_t} qp_{,i}^{n+1}n_i\,d\Gamma-\frac{\rho}{\Delta t}\int_{\Omega} q\hat{u}_{i,i}\,d\Omega \tag{5}$$

$$\int_{\Omega} w_i\frac{u_i^{n+1}-\hat{u}_i}{\Delta t}d\Omega=-\frac{1}{\rho}\int_{\Omega} w_i p_{,i}^{n+1}\,d\Omega \tag{6}$$

for all admissible functions $w\in V$, $q\in P$, where $V=\left\{w|w\in H^1(\Omega),\ w=0 \ \text{ on } \Gamma_u\right\}$,

$P = \{q \mid q \in H^1(\Omega),\ q = 0 \ \text{ on } \Gamma_p\}$, $H^1(\Omega)$ denotes the Sobolev space defined on the spatial domain Ω. In equation (4), $\bar{t}_i^u = u_{i,j} n_j$ denotes the Neumann boundary of velocity. It is important to highlight that equation (5) is a type of Poison equation [12].

2.3. Evaluation of the minor loss coefficient

The energy equation for incompressible fluid flow in a horizontal pipe is commonly expressed as follows (with the neglect of body force) [7]:

$$\left(\frac{p_1}{\gamma} + \alpha_1 \frac{v_1^2}{2g}\right) - \left(\frac{p_2}{\gamma} + \alpha_2 \frac{v_2^2}{2g}\right) = h_l + h_c \quad (7)$$

where γ is the fluid specific weight; h_1 and h_c are the major and minor energy loss per unit mass; p_1 and p_2 are the averaged static pressures over the entire cross-section; v_1 and v_2 are the average velocities; α_1 and α_2 are the kinetic energy correction factors at the upstream and downstream section, respectively.

The present study focuses exclusively on minor head losses that occur due to pipe fittings, bends, or abrupt changes in cross-sectional area, which lead to flow separation. In these cases, the major head loss (h_l) is assumed to be negligible and is therefore not considered. Minor losses, denoted by h_c , are typically characterized by a loss coefficient ζ, defined as: $h_c = \zeta \frac{v_1^2}{2g}$. The minor loss coefficient can be computed using equation (7):

$$\zeta = \frac{\left(\frac{p_1}{\rho} + \alpha_1 \frac{v_1^2}{2}\right) - \left(\frac{p_2}{\rho} + \alpha_2 \frac{v_2^2}{2}\right)}{\frac{v_1^2}{2}} \quad (8)$$

In the case of a simple pipeline expansion, the value of ζ is solely dependent on the area of sections, as noted in reference [13].

$$\zeta = \left(1 - \frac{A_1}{A_2}\right)^2 \quad (9)$$

where A_1 and A_2 are the cross-sectional areas at the upstream and downstream sections, respectively.

To calculate the major loss, we consider two cross-sections adjacent to the region of minor loss, where the flow may not be fully developed. As a result, the kinetic energy correction factors α_1 and α_2 in equation (7) are generally less than 2. These correction factors are determined using the following relation [13]:

$$\alpha = \frac{\int_A u^3 dA}{v^3 A} \quad (10)$$

3. RESULTS AND DISCUSSIONS

In this section, the finite element modeling described in Section 2.2 is employed to simulate several three-dimensional (3D) fluid flow problems. First, the algorithm is validated by comparing the results of the present code with existing benchmark data, including both experimental and numerical references. Subsequently, the FEM-based approach is applied to other common 3D geometries involving laminar flow, and the minor loss coefficient is computed for different Reynolds numbers using the formulation described in Section 2.3.

3.1. The flow past a sphere

The first benchmark problem involves flow past a sphere, which is used to validate the numerical algorithm. The schematic diagram and domain dimensions are shown in Fig. 2. A uniform velocity U_0 is prescribed at the inlet, and a no-slip boundary condition is applied on the surface of the sphere. A zero-pressure condition is imposed at the outlet, while far-field boundary conditions are applied on the remaining boundaries. The computational domain is defined with dimensions H = 12D, L = 20D, and X = 4D, where D is the diameter of the sphere and X is the upstream region [14]. Time is non-dimensionalized using the characteristic time scale D/U_0, and the Reynolds number Re is defined as follows:

$$Re = \frac{\rho U_0 D}{\mu} \quad (11)$$

For this three-dimensional case, Reynolds numbers of 100 and 400 are considered to examine steady and unsteady flows, respectively. To validate the numerical code, the drag force coefficient is used, which is calculated as follows:

$$C_d = \frac{F_x}{\frac{\pi}{8}\rho U_0^2 D^2} \quad (12)$$

where F_x denotes the total force acting on the sphere. The computational grid used for this simulation is illustrated in Fig. 3, with refined mesh elements generated near the sphere to capture flow details accurately. To assess grid independence, simulations are first performed for Re = 100 using three different mesh resolutions consisting of 124,635; 382,858, and 946,912 nodes. The resulting drag coefficients C_d for each grid,

along with comparisons to prior studies by Fornberg et al. [15], and Clift et al. [16], are presented in Table 1. Based on these results, the intermediate mesh (382,858 nodes) is selected for further simulations, as it provides a sufficiently accurate solution. The drag coefficient obtained from the present FEM-based model shows good agreement with the results reported in the literature. The steady-state solution for Re = 100 is determined using a time-matching approach, in which the solution is considered converged when no further change is observed over time. The pressure contours near the sphere and streamlines of the flow field are illustrated in Fig. 4.

The code is employed to perform simulations across a range of Reynolds numbers by varying the fluid viscosity. The computed drag coefficient C_d as a function of Reynolds number is presented in Fig. 5, along with comparisons to previously published results. It is evident that the present data show good agreement with the experimental measurements reported by Roos and Willmarth [17]. It should be noted that for unsteady flows (Re > 300), the drag coefficient is computed as a time-averaged value, while the vortex shedding frequency is characterized by the Strouhal number. For the case of Re = 400, the present study yields a Strouhal number St = 0.13, which is in close agreement with the numerical results of Kalro and Tezduyar [18] (St = 0.131) and the experimental findings of Goldburg and Florsheim [19] (St = 0.127).

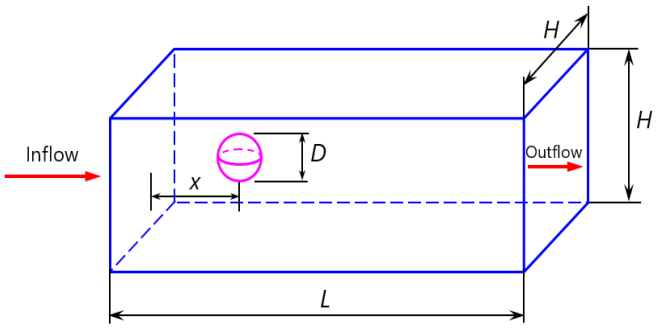

Fig. 2. Schematic of the 3D flow past a sphere

Table 1. Grid independent tests

Grids	Number of nodes	C_d
Coarse grid	124,635	1.058
Medium grid	382,858	1.084
Fine grid	946,912	1.085
Fornberg et al	-	1.085
Clift et al	-	1.087

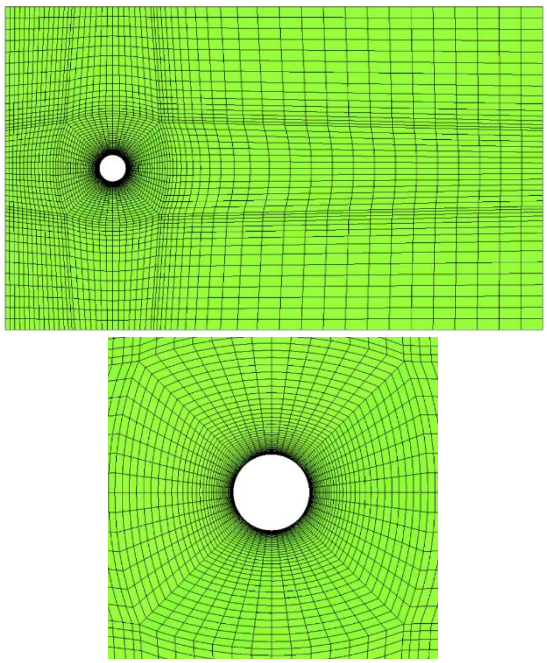

Fig. 3. Mesh near the sphere

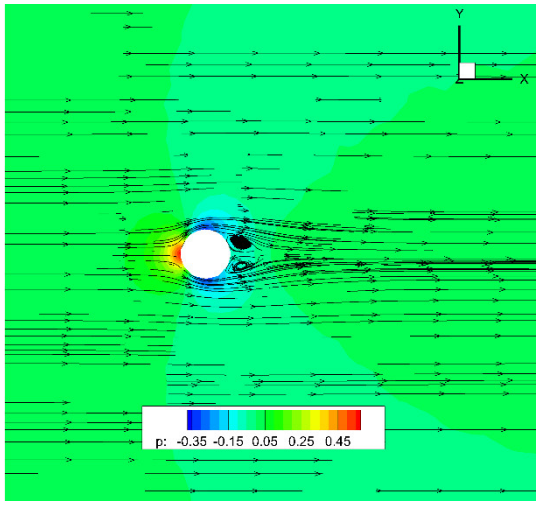

Fig. 4. Pressure contour and streamline of flow though the sphere at Re = 100

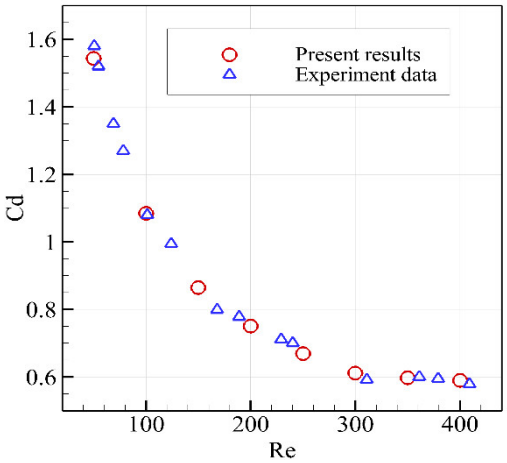

Fig. 5. Drag force coefficient versus Re number

3.2. Flow in a three-dimensional sudden expansion pipe

The second simulation investigates fluid flow through a three-dimensional (3D) pipe with a sudden expansion, as illustrated in Fig. 6, using specified geometric and boundary conditions. The inlet channel width is D = 1m, with a uniform inlet velocity of u_{in} = 0.1m/s, and a zero-pressure condition imposed at the outlet. The fluid density and dynamic viscosity are set to ρ = 1000kg/m^3 and μ = 5.0Pa.s, respectively, resulting in a Reynolds number of 20 at the inlet. A high-resolution unstructured mesh is used for this simulation (Fig. 7), comprising 82,195 nodes and 58,806 elements. The simulation is performed with a time step Δt = 0.05s, and a steady-state solution is achieved. The resulting velocity field is shown in Fig. 8, which clearly illustrates the formation of recirculating vortices downstream of the expansion region, indicative of local energy losses. Due to the sudden area change, a significant pressure drop is observed in the expansion zone.

By varying Re through adjustments in the inlet velocity, it is observed that, under fixed inlet velocity and outlet pressure conditions, the inlet pressure decreases as the Reynolds number increases. This trend arises because increasing Re implies decreasing viscosity, which results in reduced viscous resistance. Consequently, the minor loss coefficient increases, as it depends on the pressure differential at the inlet, as defined by equation (8). Additionally, higher Reynolds numbers are associated with longer and more pronounced recirculation zones within the expansion section.

The minor loss coefficient is determined from the numerical simulations and summarized in Table 2. The results indicate a decreasing trend in the coefficient as Re increases.

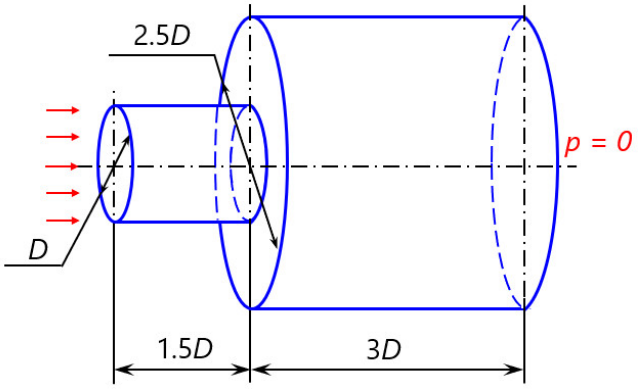

Fig. 6. 3D geometry and boundary condition of a sudden expansion problem

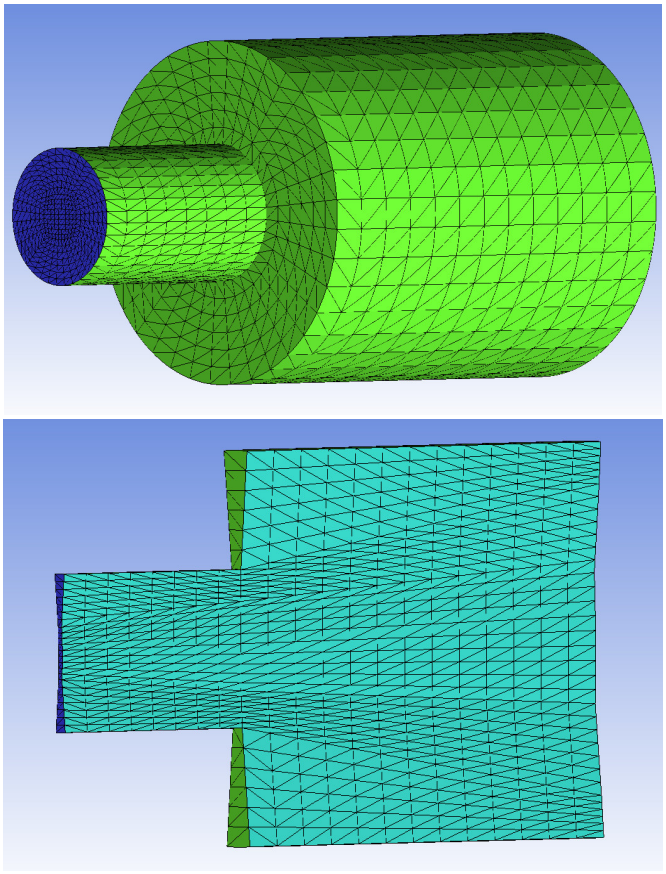

Fig. 7. Grid of a 3D sudden expansion problem

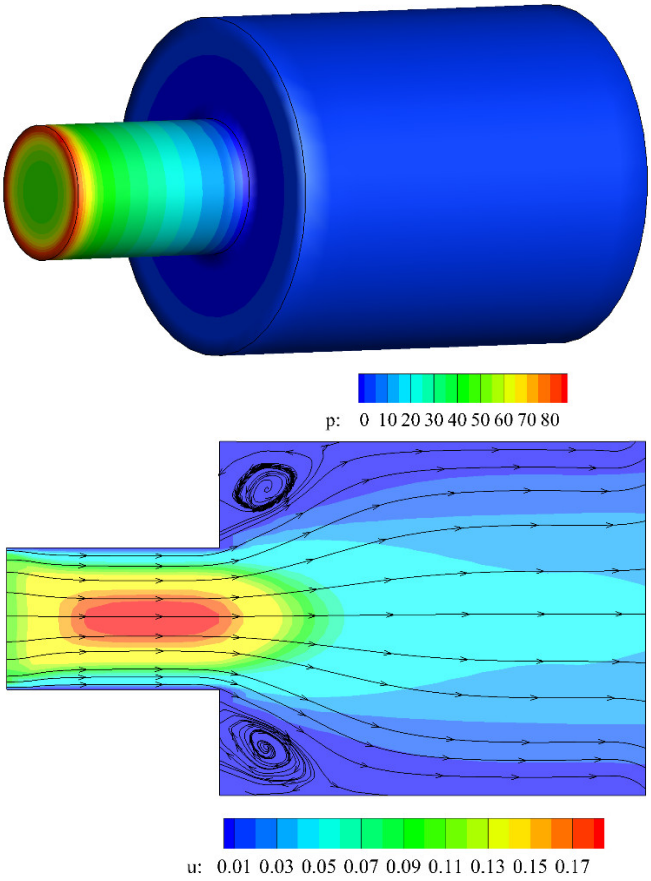

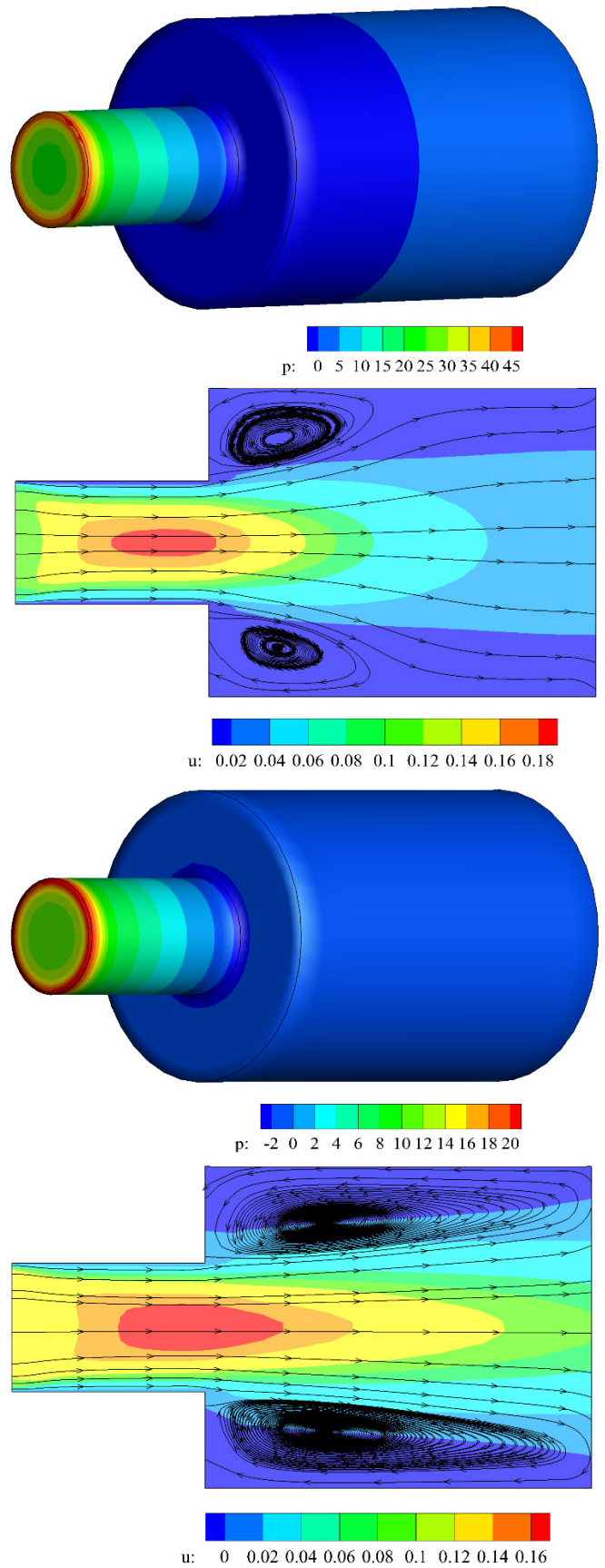

Fig. 8. Pressure contour (left) and streamline with u-velocity (right) for different Re: Re = 10 (top), Re = 20 (middle), Re = 50 (bottom)

Table 2. The minor loss coefficient ζ obtained by numerical solution

Re	10	20	50	100	200
ζ	11.8	6.4	3.3	2.4	1.9

3.3. Flow in a three-dimensional 90-degree bend

Lastly, the FEM model is employed to simulate fluid flow in a three-dimensional 90-degree bend (elbow). The geometry of this benchmark test case, as described in Refs. [20, 21], is illustrated in Fig. 9. The pipe has a diameter of D = 4mm and a curvature radius of R = 16mm. A tetrahedral mesh is used for this 3D simulation, as shown in Fig. 10. Due to symmetry, only half of the domain is simulated. A grid independence test is conducted, and the comparison of the velocity component in the y-direction for three mesh resolutions (coarse, medium, and fine) is presented in Fig. 11. The medium-resolution grid is selected for subsequent simulations, as it provides sufficient accuracy with reasonable computational cost.

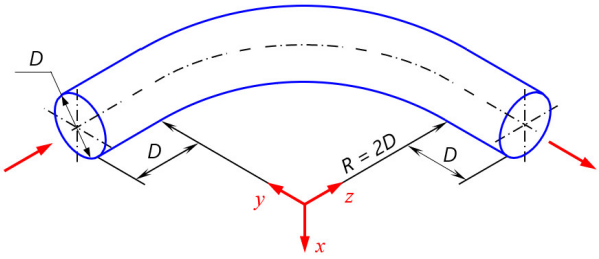

Fig. 9. Geometry of a curved pipe

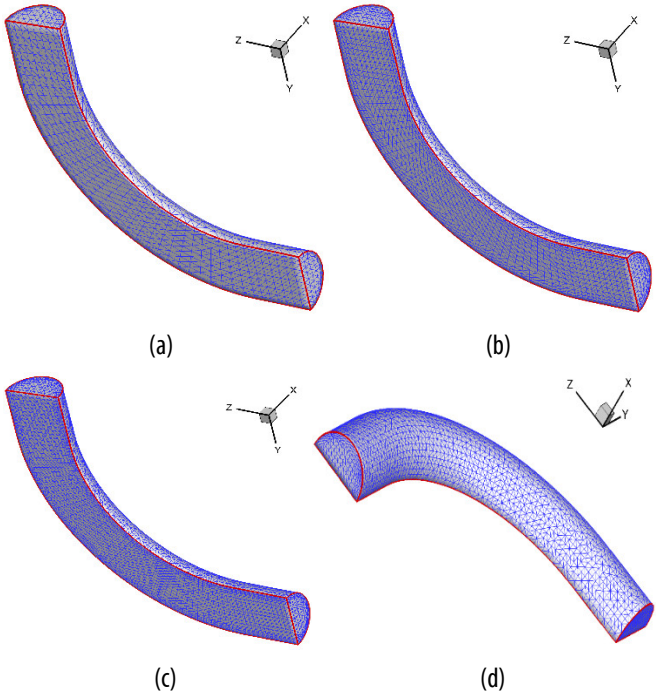

Fig. 10. Tetrahedral grids for curved pipe problem: (a) coarse grid, (b) medium grid, (c) and (d) fine grid

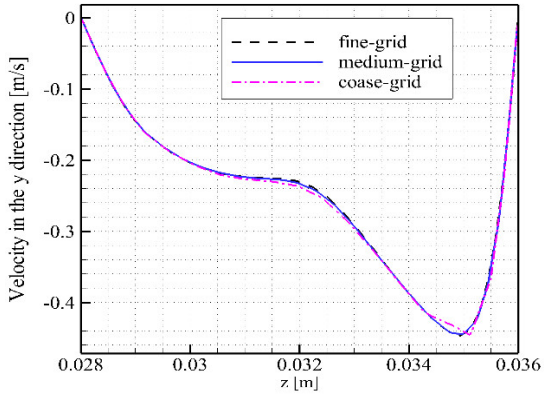

Fig. 11. Velocity in y component for test grid

The simulation is performed until a steady-state solution is achieved. At the inlet, a fully developed velocity profile is applied, and the Reynolds number is set to Re = 300. The velocity distribution along the centerline of the mid-plane cross-section (from the inner to the outer wall) is shown in Fig. 12. The present results show good agreement with both the experimental data and the numerical results reported in Ref. [21].

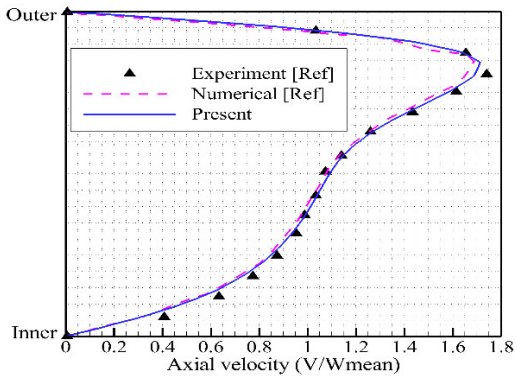

Fig. 12. Validation of steady flow (Re = 300)

A steady-state solution is achieved, and the corresponding pressure contours are illustrated in Fig. 13. The minor loss coefficients, computed from the numerical simulations, are summarized in Table 3. As observed in the case discussed in Section 3.2, the loss coefficient exhibits a decreasing trend with increasing Re.

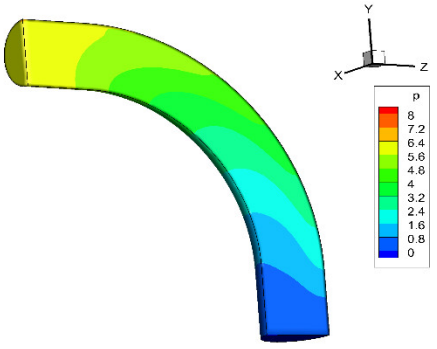

a)

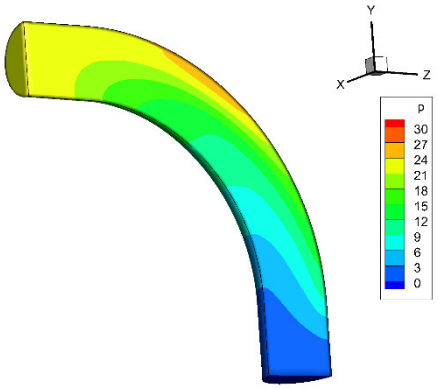

b)

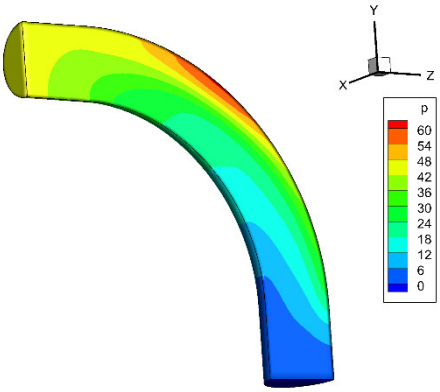

c)

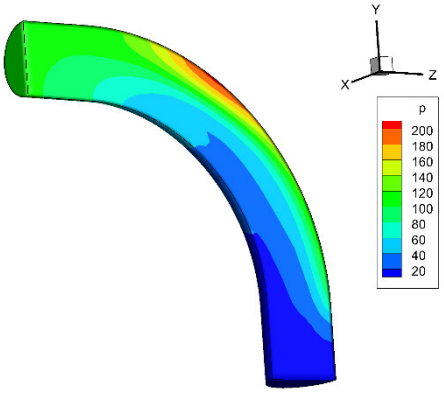

d)

Fig. 13. Pressure contour versus Re:
(a) Re = 100, (b) Re = 300, (c) Re = 500, (d) Re = 1000

Table 3. The minor loss coefficient ζ obtained by numerical solution

Re	100	300	500	1000
ζ	5.04	2.12	1.41	0.83

4. CONCLUSION

This study demonstrates the effectiveness of the finite element method (FEM) in simulating minor head losses in three-dimensional flow domains. The numerical approach was validated against classical benchmark cases and subsequently applied to more complex

geometries, including sudden expansions and 90-degree pipe bends.

The key findings are as follows:

- FEM implemented on unstructured tetrahedral/ hexahedral meshes accurately captures flow separation and pressure drops in complex 3D geometries.

- The computed minor loss coefficient decreases with increasing Reynolds number, in agreement with theoretical and experimental expectations.

- The proposed simulation framework offers both flexibility and accuracy, making it suitable for the analysis and design of hydraulic components in industrial applications.

The results confirm that extending FEM analysis from two-dimensional to three-dimensional configurations offers enhanced insight into loss mechanisms and contributes to the optimization of hydraulic component design. Future research will focus on extending the methodology to turbulent and transient flow regimes, as well as exploring GPU-accelerated computing to improve efficiency in large-scale models.

REFERENCES

[1]. Gorla C., Carlo F., Stahl K., Höhn B. R., Michaelis K., Schultheiß H., Stemplinger J.P., "Hydraulic losses of a gearbox: CFD analysis and experiments," *Tribology International,* 66, 337 - 344, 2013.

[2]. Guo M., Miao S.H., Tang X.L., Zuo Z.G., Li X.Q., "Evaluation of shaft forces in a vertical canned motor through local hydraulic loss analysis," *Advances in Mechanical Engineering,* 10.3, 1687814018765599, 2018.

[3]. Abd H.M., Alomar O.R., Mohamed I.A., "Effects of varying orifice diameter and Reynolds number on discharge coefficient and wall pressure," *Flow Measurement and Instrumentation,* 65, 219 - 226, 2019.

[4]. Sondh H.S., Singh S.N., Seshadri V., Gandhi B.K., "Design and development of variable area orifice mete," *Flow Measurement and Instrumentation,* 13.3, 69 - 73, 2002.

[5]. Seetharaman S., Kahraman A., Moorhead M.D., Petry-Johnson T.T., "Oil Churning Power Losses of a Gear Pair: Experiments and Model Validation," *Journal of Tribology,* 131(2), 022202, 2009.

[6]. Chemezov D., "The character of the fluid flow in the pipelines with the local hydraulic resistances," *ISJ Theoretical & Applied Science*, 12 (44), 62 - 68, 2016.

[7]. Weber J., Facas G.N., Horst M., Sharobeam M., "Using FLUENT to Supplement Theory in an Introductory Fluid Mechanics Course," *International Journal of Hydraulic Engineering,* 8(1), 11 - 21, 2019.

[8]. Nguyen M.H., Ha T.S., "Minor head loss analysis of laminar fluid flow in complex geometries," *Journal of Science and Technique*, 18(03), 5-18, 2023.

[9]. Ha S.T., Choi H.G., "Semi-monolithic formulation based on a projection method for simulating fluid–structure interaction problems," *Computers & Mathematics with Applications*, 134, 207-224, 2023.

[10]. Ha T.S., Vu V.C., Nguyen M.H., Nguyen M.D., "Numerical simulation for fluid-structure interaction of a blood flow with the aortic valve using the fem monolithic formulation," *Journal of Science and Technique*, 16(03), 49-60, 2021.

[11]. Ha S.T., Choi H.G., Long N.C., Lee S.W., "A semi-implicit finite element formulation of the partitioned method for fluid-structure interaction based on a flux boundary condition of pressure equation," *Journal of Mechanical Science and Technology*, 37(5), 2417-2424, 2023.

[12]. Ha S.T., Choi H.G., "A meshless geometric multigrid method based on a node-coarsening algorithm for the linear finite element discretization," *Computers & Mathematics with Applications,* 96, 31-43, 2021.

[13]. Pritchard P. J., Mitchell J. W., *Introduction to Fluid Mechanics,* 9th Edition, Wiley, 2015.

[14]. Lee S., "A numerical study of the unsteady wake behind a sphere in a uniform flow at moderate Reynolds numbers," *Computers & Fluids*, 29(6), 639-667, 2000.

[15]. Fornberg, B., "Steady viscous flow past a sphere at high Reynolds numbers," *J Fluid Mech,* 190, 471-89, 1988.

[16]. Clift R., Grace J.R., Weber W.E., *Bubbles, drops, and particles.* New York: Academic Press, 1978.

[17]. Roos F.W., Willmarth W.W., "Some experimental results on sphere and disk drag," *AIAA journal*, 9(2), 285-291, 1971.

[18]. Kalro V., Tezduyar T., "3D computation of unsteady flow past a sphere with a parallel finite element method," *Comp Methods in App Mech Eng*, 151, 267-76, 1998.

[19]. Goldburg A., Florsheim B.H., "Transition and Strouhal number for the incompressible wake of various bodies," *Phys Fluids*, 3(1), 45-50, 1996.

[20]. Van de Vosse F.N., Van Steenhoven A.A., Segal A., Janssen J.D., "A finite element analysis of the steady laminar entrance flow in a 90^0 curved tube," *International journal for numerical methods in fluids*, 9.3, 275-287, 1989.

[21]. Rindt C.C.M., Van Steenhoven A.A., Janssen J.D., Vossers G., "Unsteady entrance flow in a 90^0 curved tube," *Journal of Fluid Mechanics*, 226, 445-474, 1991.